Check for updates

Cryogenic Focused Ion Beam Milling to Investigate the Anisotropic Magnetotransport Properties of Bismuth Microcrystals

Amaia Sáenz-Hernández, Soraya Sangiao, Claudia Felser, Chandra Shekhar, José Ángel Pardo, Alfonso Ibarra, and José María De Teresa**

Bulk single crystals exhibit the intrinsic properties of a given compound, but studying their anisotropic magnetotransport properties is challenging. Focused Ion Beam (FIB) milling at room temperature has been previously used to guide the electrical current path along a defined crystal direction or to extract microcrystals where the electrical current flows along a known direction. However, some materials, such as bismuth, melt under FIB irradiation. Bismuth, known for its unique properties, including very large magnetoresistance and a highly anisotropic Fermi surface, reacts to room-temperature Ga^+ FIB irradiation, forming droplets on its surface. Therefore, a novel microfabrication approach based on cryogenic FIB milling is developed here. By using a Peltier stage or an integrated cryogenic module, surface melting is mitigated below −30 °C. Microscale slabs are extracted, either parallel or perpendicular to the single crystal surface, then shaped and electrically contacted in a chip for magnetotransport characterization. The large magnetoresistance observed along with Shubnikov–de Haas oscillations with single periodicity when current is applied perpendicular to the *c* axis, highlights the success of the approach. These results enable FIB microfabrication of single crystals that are sensitive to FIB irradiation and investigation of the anisotropic magnetotransport properties in microcrystals.

1. Introduction

The study of quantum materials is of fundamental importance due to their rich emergent phenomena, which arise from strong electron interactions, spin-orbit coupling, and topological effects. Understanding and controlling the properties of quantum materials paves the way for the next generation of quantum devices, including quantum sensors and quantum computers.[1,2]

In particular, a comprehensive understanding of the anisotropy in the electrical transport properties in quantum materials is essential for advancing our knowledge of their behavior. It is well established that the magnetotransport properties of single crystals strongly depend on the relative orientation of the current and the applied magnetic field, as well as the crystallographic axes.[3–7] However, accurately measuring this anisotropy in bulk crystals remains challenging due to limitations imposed by their size and shape. These factors often lead to the presence of large-scale defects and hinder the ability to draw conclusions due to the spatial variation of the direction of the applied current.

Bismuth stands out among quantum materials due to its unique fundamental electronic properties: It exhibits an exceptionally low carrier density and small effective mass, which enhance quantum effects even at relatively high temperatures and moderate magnetic fields. Its strong spin-orbit coupling makes it an ideal candidate for exploring spin-related phenomena and topological phases.[4,7,8] It has recently been determined to be a second-order topological insulator, as evidenced by the observation of topological states in 2D films and in the edges of cleaved surfaces in bulk bismuth.[9–11] Additionally, it has played an important role in the discovery of key quantum phenomena, including the Shubnikov–de Haas oscillations and the de Haas–van Alphen effect.[12,13] Several interesting properties of this material are attributed to its highly anisotropic Fermi surface, formed by an ellipsoidal hole pocket at the Brillouin zone T point, with its long axis aligned along the trigonal axis, and three ellipsoidal electron pockets positioned at the L points, separated by a $2\pi/3$ interval. It has been demonstrated that, owing to the structural characteristics of the Fermi surface, the magnetotransport properties of bismuth exhibit variability across different

A. Sáenz-Hernández, S. Sangiao, J. Á. Pardo, A. Ibarra, J. M. De Teresa
Instituto de Nanociencia y Materiales de Aragón (INMA)
CSIC-Universidad de Zaragoza
Zaragoza 50009, Spain
E-mail: sangiao@unizar.es; deteresa@unizar.es

S. Sangiao, J. Á. Pardo, A. Ibarra
Laboratorio de Microscopías Avanzadas
Universidad de Zaragoza
Zaragoza 50018, Spain

C. Felser, C. Shekhar
Max-Planck-Institute for Chemical Physics of Solids
01187 Dresden, Germany

J. Á. Pardo
Departamento de Ciencia y Tecnología de Materiales y Fluidos
Universidad de Zaragoza
Zaragoza 50018, Spain

The ORCID identification number(s) for the author(s) of this article can be found under https://doi.org/10.1002/adfm.202517475

DOI: 10.1002/adfm.202517475

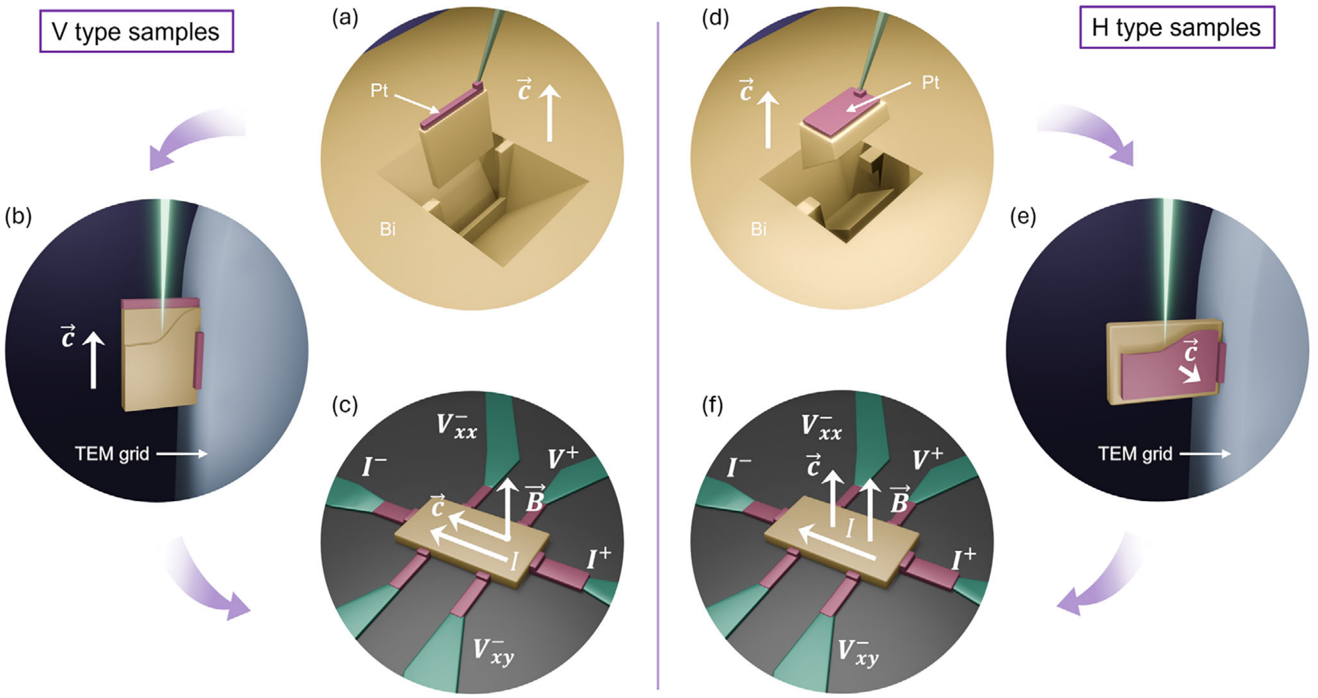

Figure 1. Computer-generated images that schematize and compare the three main steps of the fabrication processes for V and H samples. Panels a–c) correspond to type V and d–f) to H. First, a bismuth (yellow) microcrystal is extracted from a macroscopic single crystal covered by a platinum (pink) protective layer (panels (a and d)). Then, it is transported to a TEM grid (gray) for shaping. After polishing the microcrystal into a slab with a thickness of ≈1 µm (panels (b and e)), it is moved to a silicon dioxide chip with gold leads (green), where Pt is deposited by FIBID to allow magnetoresistance measurements. The bonding plan is shown in the bottom images, which also indicate the directions of current flow, the ***c***-axis, and the applied magnetic field (panels (c and f)).

crystallographic directions, which will be the focus of the present study.[4,8,14,15]

A variety of techniques have been developed over the years to address the challenge of studying the anisotropy in the electrical transport properties in quantum materials, which involve the study of microscale single crystals from bulk materials. Focused Ion Beam (FIB), a direct-write nanolithography technique, has become one of the most used for sample preparation due to its versatility and capacity to process materials with non-planar and complex geometries at nanometric resolution.[16,17] With FIB, material cutting and shaping are possible via the milling caused by the impact of the ions with the sample surface, where atoms are ejected if the impact energy exceeds their binding energy. Additionally, in combination with a precursor material, usually in gas form, ions can be used to deposit materials in a technique called Focused Ion Beam Induced Deposition (FIBID).[18]

In the pursuit of advanced techniques for microcrystal characterization, FIB and FIBID have been widely adopted by several research groups. In certain studies, FIB technologies are employed to pattern microcrystals for specific experimental configurations.[19–23] In other cases, it is employed to directly extract microcrystals from bulk material for subsequent analysis.[24–27] This process is typically part of an ex situ process that integrates additional techniques for contact placement. Other research groups have also developed microcrystal extraction techniques that employ FIB to study surface properties of single-crystal materials.[28]

Our group has previously proposed two extraction processes that use Ga^+ FIB technologies exclusively.[29,30] These processes enable, on one hand, the fabrication of hybrid devices that integrate superconductors with topological insulators, and on the other hand, the detailed characterization of anisotropic electrical transport properties with precise placement of contacts, avoiding techniques that rely on chemical resists. The entire process is carried out in situ while being monitored in real time using a Scanning Electron Microscope (SEM), ensuring a high degree of control over the process. These methods, which were tested on a Bi_2Se_3 single crystal, are used to extract microcrystals in two different orientations, horizontal (H) and vertical (V), following the process illustrated in **Figure 1**. For V samples, the microcrystal slab is extracted with its largest surface parallel to the crystallographic axis ***c*** (Figure 1a), whereas, in H samples, the largest surface is perpendicular to the vector ***c*** (Figure 1d). After being polished and shaped into slabs (Figure 1b,e) and subsequently mounted on a silicon dioxide chip, both samples are contacted with different relative directions of the current flow and the applied magnetic field with respect to ***c*** (Figure 1c,f). These devices facilitate the characterization of anisotropic magnetotransport properties and can be further processed for the fabrication of more complex devices, such as their combination with superconducting structures.[29]

The present work builds upon the previously developed methodologies, adapting them for the extraction of bismuth microcrystals to produce V and H type devices. Initial tests show that this material is FIB sensitive, melting under irradiation, a

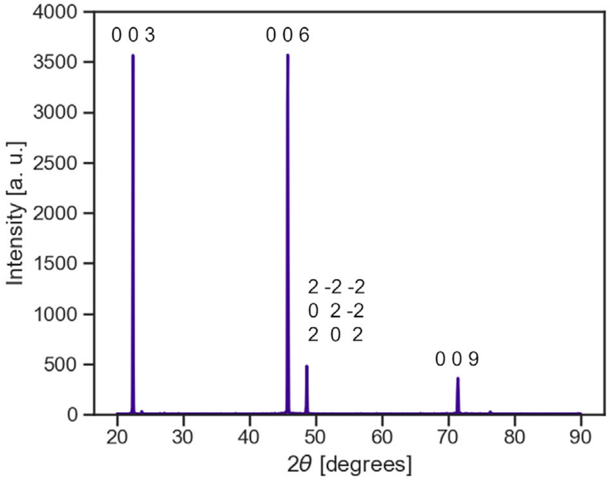

Figure 2. $\theta/2\theta$ XRD scan of the macroscopic Bi crystal used for microcrystal extraction.[31]

problem that is solved by the implementation of cryo-FIB milling. The longitudinal resistivity as a function of temperature and magnetic field are characterized for devices of both orientations, revealing the presence of Shubnikov-de Haas oscillations. Our results show clear evidence of anisotropic electrical transport properties and demonstrate a reliable methodology for sample fabrication.

2. Results and Discussion

In addition to device fabrication, several structural characterization processes were carried out to ensure the crystalline quality of the produced samples. This section details the methodologies employed and the results of the structural characterization, along with the description of the implementation of cryo-FIB milling to the fabrication process. Finally, the results of the magneto-transport measurements are presented, providing insight into the electronic properties of the microscale single crystal devices.

2.1. Characterization of the Starting Bi Crystal

The samples studied in this work were extracted from a Bi single crystal that was synthesized by the Bridgman method and belongs to the space group R-3m (166).

The crystal dimensions are $\approx 1 \times 0.5 \times 0.3$ cm^3. It was cut so as to present a flat surface perpendicular to the growth direction. X-ray diffraction (XRD) experiments were performed to determine its crystal structure and orientation. A $\theta/2\theta$ scan measured with the scattering vector perpendicular to the flat surface is shown in **Figure 2**. It proves that the crystal grows preferentially along the [001] direction (trigonal c axis). However, a weak reflection corresponding to a secondary orientation is observed, proving that minor crystalline domains with a different orientation are present. The slabs for the magnetotransport anisotropy measurements were then extracted from this crystal following the procedure described before. These XRD results ensure that there is a high probability of extracting single-crystal slabs from this bulk crystal.

2.2. Low-Temperature Fabrication of Bi Microcrystal-Based Devices

Initial attempts for crystal extraction were done using Ga$^+$ FIB at room temperature, based on the process described in references,[29,30] while monitoring in real-time SEM, which is integrated in the equipment. The apparition of liquid droplets was observed when irradiating the crystal at different currents at an acceleration voltage of 30 kV (see Section S1 and videos S1 and S2, Supporting Information for additional details). To avoid this issue, the fabrication process has required significant modifications.

A similar phenomenon was previously reported for group III–V semiconductors and was effectively mitigated by fabricating at low temperatures.[32–34] Therefore, we have implemented two alternative techniques that lower the crystal temperature during the Ga$^+$-FIB milling steps. The first technique uses a cooling stage designed for SEM and FIB sample chambers that are equipped with a Peltier plate for temperature control. The second technique employs an N$_2$-based cryo-module integrated into the system. These two methods, which are compared in **Table 1**, will be referred to as the P (Peltier) and C (cryo) methods, represented in the schematics in **Figure 3a,b**, respectively. Two samples of each type (H and V) are shown here, each fabricated using either the P or C method. Hereafter, they will be referred to as H-P, H-C, V-P, and V-C. The selected samples are considered the most representative of their respective categories. In total, at least two samples of each of the four types were studied, showing reproducible results.

In method P, the cooling stage can reach a minimum temperature of −60 °C, whereas the cryo-module can reach −150 °C. Since no melting was observed visually below −30 °C (as described in the Supporting Information), the aim was to determine whether the −60 °C provided by the cooling stage was sufficient, or if further lowering the temperature with the cryo-module (C method) would improve the quality of the extracted micro-crystals. Both P and C methods have been applied to fabricate V and H sample types. The room-temperature fabrication of V and H samples have been previously reported,[29,30] therefore only the variations introduced by the use of the cooling stage and the cryo-module will be discussed hereafter.

The Bi crystal and a TEM grid holder with a copper grid are placed in the processing chamber in the correct position for H or V sample fabrication (lying flat in the case of H samples and standing upright for V samples). They are fixed to a sample holder (a small and thin metallic piece to improve thermal conductivity between the stage and the introduced elements) via carbon tape, ensuring good thermal contact between these elements and the sample holder. This is especially important when using the cooling stage, because it has problems lowering the temperature when the stage holder and the introduced elements are relatively large.

The described fabrication process is applicable to both P and C methods, though there are subtle differences in the steps. Due to the low temperature reached, the cryo module comes with an anti-contaminator, which is set at a temperature lower than the stage to trap any impurities that might otherwise condense on the cold surfaces. When using the cryo-module to lower the temperature, it is typically set to −150 °C, with the anti-contaminator

Table 1. Summary and comparison of both cryo-FIB milling methods (P and C) tested for fabrication.

	P method	C method
Equipment	Peltier plate	N_2-based cryo-module
Minimum temperature	−60 °C	−150 °C
Advantages	Fast and easy to operate	Allows cryo-FIB in a wider range of temperatures
Limitations	Due to the narrow temperature range, some materials may not be suitable for manipulation using this technique.	Slow. Mechanical limitations when rotating the stage

maintained at −175 °C to minimize contamination. As mentioned above, when the Peltier plate is used instead, the temperature is set to −60 °C, a value easily reached if the sample holder is properly prepared. In both cases, once the temperature sensor reaches the desired value, the system is left to stabilize for a few minutes to ensure that all elements on the sample holder are cold enough.

Platinum deposition by FIBID must be carried out at room temperature, therefore, the process involves decreasing and increasing the temperature several times depending on the fabrication step. The temperature is first lowered after the protective Pt layers are deposited. The microcrystal is shaped and partially separated from the bulk crystal by FIB milling at low temperature to leave it fixed until it is attached to the nanomanipulator with a Pt deposit. Therefore, for this step, the stage is returned to room temperature.

The next step is to finish cutting the microcrystal in order to fully separate it for transport to the TEM grid. However, drifting may occur when cooling the system down to make this cut, which could break the nanomanipulator. Therefore, this last milling step is done at room temperature, despite the risk of melting. To prevent damage to the microcrystal, the cut is made with enough space left between it and the Pt-protected region. Transmission electron microscopy (TEM) shows that these fast cuts do not cause a relevant damage to the crystal when made at room temperature (see section 2.3).

The microcrystal is then transported and fixed to the grid. When the nanomanipulator is detached and withdrawn from the chamber, the temperature is lowered one last time for shaping and polishing the microcrystal into a very thin slab. In the case of the C method, it must be noted that tubes transporting cooled gas hinder the rotation of the stage. This forces the user to polish one of the sides of the slab blindly, without the possibility of checking the process with the SEM.

Once this step is finished, the system is set to room temperature, as subsequent fabrication steps involve the use of the nanomanipulator and Pt deposition. At one last milling step, the nanomanipulator is detached from the slab at room

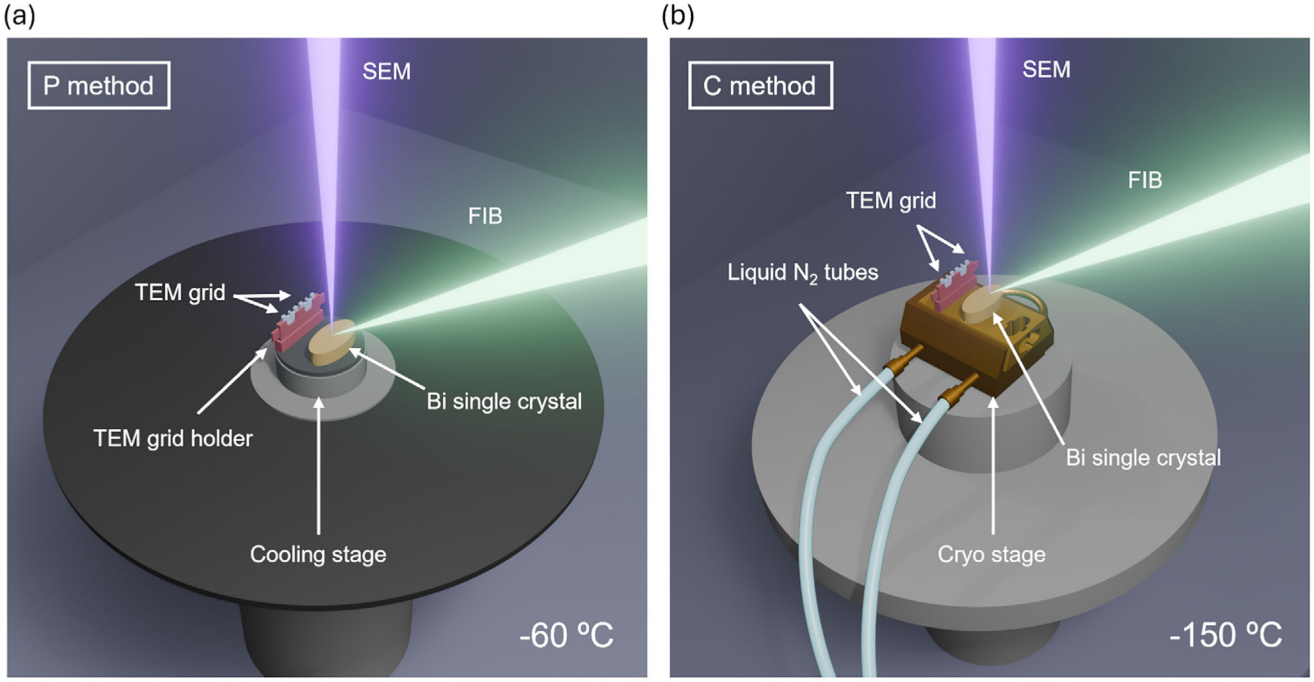

Figure 3. Computer-generated images of the two setups used for the different low-temperature fabrication methods: a) P, with the cooling stage, and b) C, using the cryo-module. Both images show the starting point for V sample fabrication. For H devices, the TEM grid is tilted 90°, lying on top of the sample holder.

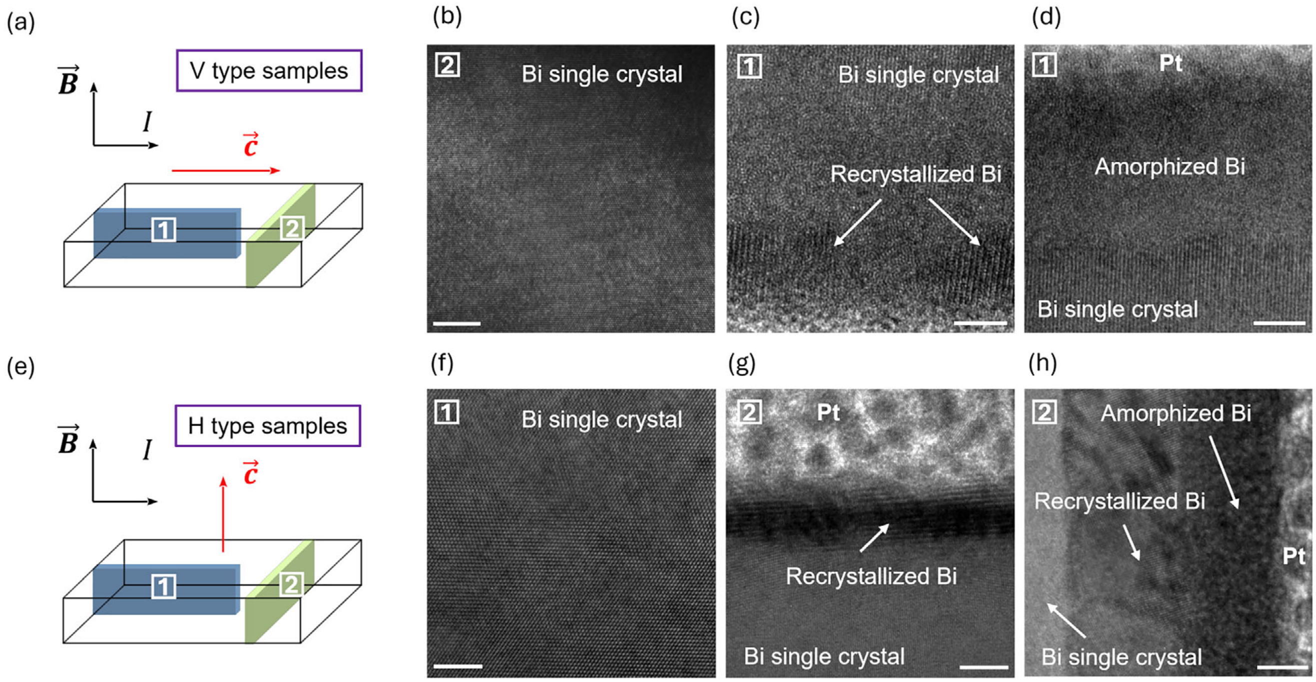

Figure 4. Scheme of the orientation of the extracted lamellae and HRTEM micrographs of a) V-P and e) H-C. Upper panels b–d) correspond to micrographs of sample V-P, and the lower panels f–h) to H-C. Numbers on the micrographs indicate the corresponding lamellae orientation. Panels (b,f) correspond to the centers of the lamellae and c,d,g,h) to the edges. Scale bar is 5 nm. Micrographs for other samples can be found at the Supporting Information.

temperature and low currents (24 pA) to reduce the impact of the bubble formation.

This section describes the fabrication process used for the reported samples in the manuscript. For future experiments, the process could be optimized further by implementing a tilted sample holder that can fit all the fabrication elements needed, be thin enough to be cooled by the Peltier module, and avoid the need to open the chamber to tilt the TEM grid holder.

2.3. Structural Characterization of the Devices

To draw conclusions from the magnetotransport results, it is necessary to know the exact crystallographic structure of the devices. As observed in XRD experiments, the Bi crystal consists of grains with different crystallographic structures that preferentially grow along the trigonal *c* axis. Even if the Bi crystal is predominantly a single crystal, the results of the XRD experiments showed reflections indicating a minor presence of grains with varying crystallographic orientations. Therefore, additional structural characterization experiments are conducted to ensure that the studied microcrystals were not extracted from a region near a grain boundary. Additionally, Ga^+ FIB irradiation is known to cause amorphization and contamination by ion implantation in processed specimens; therefore, it is essential to assess the extent of this damage.

For this reason, the samples were analyzed using high-resolution transmission electron microscopy (HRTEM). After characterizing the magnetotransport properties of the fabricated devices, two lamellas were extracted from each microcrystal in two different directions. A scheme of the lamella extraction orientation for each device type and some HRTEM micrographs for V and H samples are displayed in **Figure** 4a,e respectively. Electron diffraction patterns were taken at the center of each lamella (Figure 4b,f) to determine the crystal planes, verifying that the *c* axis is in the correct orientation for every sample studied. They were also proven to be mostly composed of the rhombohedral structure with the main orientation of the original single crystal, with the exception of V-C where a small grain of another orientation was observed.

Two different regions of damage were noted. Some regions of the slab's surface are amorphous, while in others, the damaged areas have recrystallized, forming small crystalline grains (see Figure 4c,d,g,h, and Section S2, Supporting Information). These recrystallized areas are attributed to milling steps performed at room temperature during fabrication. During these steps, some melting occurred due to the local increase in temperature caused by ion irradiation. As the damaged regions gradually cooled, they recrystallized into small grains. When these steps are performed at low temperatures, the local temperature decreases, preventing recrystallization and resulting in amorphized areas.

It was observed that ions penetrated an average of 15 nm in V samples. The total damaged volume represented just 4% of the total measured volume in the magnetotransport experiments. Due to the extraction process, H samples are slightly more damaged. One side of the slab shows greater damage, up to 70 nm in the thickest region. The damage gradually narrows along the slab's surface, reaching a thickness of 5 nm in some areas. Even considering an average damage depth of 40 nm, it would

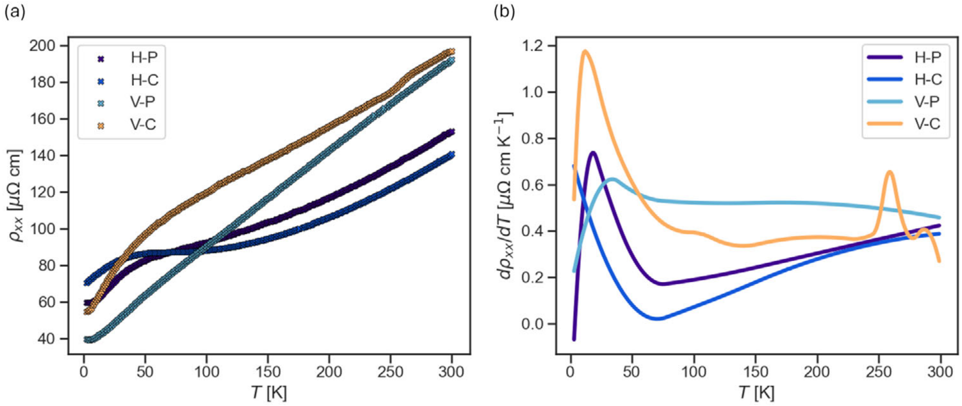

Figure 5. a) Longitudinal resistivity as a function of temperature of the devices. Data was collected during a slow cooldown from 300 to 2 K using a 10 µA probe current. b) First derivative of the ρ_{xx}(T) experimental data, interpolated and smoothed using a Savitzky–Golay filter for clarity.

represent less than 10% of the total measured volume. At low temperatures, the mean free path of bismuth is of the order of a few microns, which is relatively similar to the dimensions of the slab.[7,35] A reduction of the length, width, and thickness of the single crystal due to amorphization would mean a reduction of the mean free path of the carriers. As the magnetic field is later applied parallel to the thickness, the most relevant dimensions for magnetotransport studies are length and width. For V-type samples, where the damage depth is an average of 20 nm at each side, the reduction would be 40 nm in total. H-type samples are the most affected by damage, including the 70 nm damage on one side and the 20 nm at the opposite, the total reduction of the width of the single crystal can be ≈100 nm. A size reduction of 100 nm, although small compared to the mean free path, which is on the order of several microns, will still limit the carrier orbits at high magnetic fields, and therefore slightly reduce the maximum MR achievable, particularly at low temperatures.

Regarding contamination, minimal ion implantation occurred, as no Ga was detected by energy-dispersive X-ray spectroscopy (EDS) in the damaged regions (see Section S3, Supporting Information).

Based on this analysis, it was concluded that the magnetotransport measurements reported in the following section accurately represent the bulk transport properties along different crystallographic directions, and we note that no particular difference was observed between C and P devices.

2.4. Magnetotransport Properties of Bi Devices Fabricated Along Two Perpendicular Crystallographic Directions

2.4.1. Longitudinal Resistivity as a Function of Temperature and Magnetic Field

This section summarizes the magnetotransport measurements performed on the four samples, each labeled with a two-letter code, as previously described. The four of them have a similar shape, with their thickness ranging between 1–1.2 µm, the width between 3–6 µm, and the length between 6.5 to 8.5 µm. The silicon dioxide chips containing the devices are bonded to a Physical Properties Measurement System (PPMS) puck, as indicated in Figure 1, using a four-probe configuration. The magnetic field B is oriented perpendicular to the direction of the current flow.

Samples exhibit a metallic behavior, as shown in **Figure 5a**, where the longitudinal resistivity ρ_{xx} is plotted as a function of the temperature T in the range of 2 to 300 K with the data taken during a slow cooldown at 0 T. The temperature coefficient $d\rho_{xx}/dT$, plotted in Figure 5b, remains positive along the full range, as it is expected from bulk Bi.[36] For H samples, the decrease in the slope is linear until the temperature reaches 100 K. At this point, a change in the behavior is observed, where the slope for H-P stabilizes before rapidly descending to zero at 50 K, and the slope of H-C smoothly descends to 0 at 50 K. In the case of V samples, the temperature coefficients remain constant from 300 K to 100 K. For every sample, an increase in the slope is observed between 30 and 10 K, which is less pronounced in the case of V-P. Below 10 K, ρ_{xx} decreases quickly and stabilizes. However, an exception to this trend is observed for the V-P sample, where this effect may have occurred at lower temperatures (below 2 K). This alteration in behavior, occurring at ≈100 K, is attributed to the modification of the mean free path. At 300 K, the mean free path is of the order of a few nanometers. As temperature decreases, it increases, reaching the micrometer scale ≈100 K and becoming comparable to the device dimensions. At this point, the slab thickness limits the mean free path, leading to a change in the temperature coefficient. Additionally, for single-crystal devices of similar dimensions, calculations show that the dominant scattering mechanism between 100 and 300 K is phonon scattering. Due to the changes in mean free path, ion impurity scattering starts gaining importance, quickly becoming the main scattering source below 50 K.[7,37–40] Moreover, this behavior has been reported to be similar across different crystallographic directions, which explains the lack of differences in ρ_{xx}(T) curves observed among the samples. The reported behavior for ρ_{xx} and the temperature coefficient has also been experimentally observed by Hasegawa et al. and Otsuka et al., who report a peak in the temperature coefficient ≈20 K, with a subsequent rapid decrease in nanowires with widths comparable to those of our devices.[35,38]

The dependence of ρ_{xx} with the applied magnetic field B at 2 K is displayed in **Figure 6a**. The set of data was collected by sweeping the magnetic field from −14 to 14 T, with each data point computed as the average of five measurements taken at each field

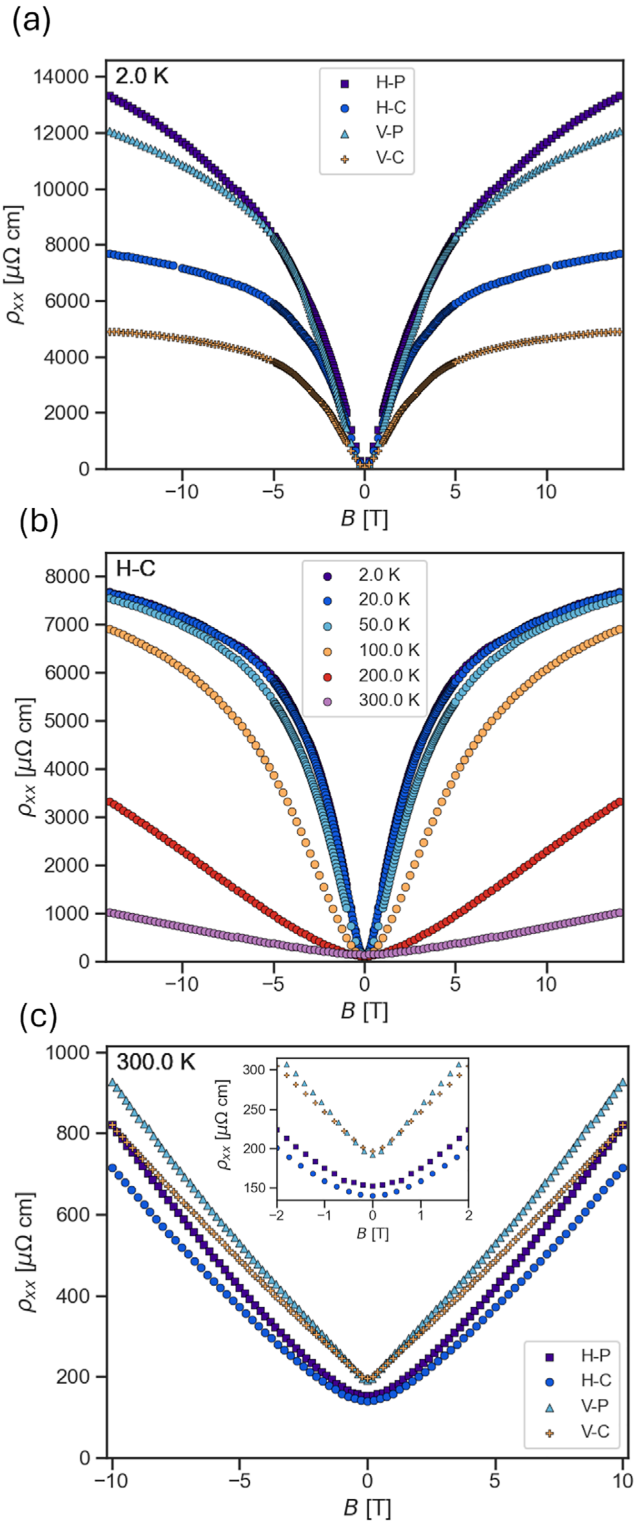

Figure 6. a) Longitudinal resistivity ρ_{xx} dependence on the magnetic field at 2 K for each sample. b) ρ_{xx} dependence on the magnetic field of device H-C at different temperatures. c) $\rho_{xx}(B)$ at 300 K for the different devices, showing differences between the transport properties of V samples and H samples from −2 to 2 T, highlighted in the insert.

value. The data has been treated to remove any contributions from the antisymmetric Hall resistivity by averaging the measurements at opposite magnetic field values. In Figure 6b, the evolution of the curve with temperature for sample H-C is plotted. Similar behavior is observed in the other samples (Supporting Information). When the temperature increases, the shape of the $\rho_{xx}(B)$ curve changes, becoming a parabola over 100 K (See Section S4, Supporting Information), an effect once again related to the change in the value of the mean free path. Figure 6c shows the $\rho_{xx}(B)$ curves at 300 K, exhibiting a parabolic trend and a clear difference between H and V samples. The latter exhibits a small inverse peak from −1 to 1 T, which is absent in the H samples, where a broader parabola is observed. This change in behavior at higher temperatures has also been reported by Chien et al. where a broad parabola is reported at high temperatures for H type samples.[7]

Magnetoresistance (MR) values were calculated as the percentage change in longitudinal resistivity relative to the resistivity at zero field. At 2 K and 14 T, the following MR values were obtained: V-P exhibits a resistivity change of 30000%, followed by H-P with 21500%, H-C with 10700%, and V-C with 9000%. At 300 K the MR is greatly reduced, ranging between 400% and 700%. This agrees with reported values for bulk bismuth, which is known for its large magnetoresistance.[7,41] It must be noted that MR values are limited by the dimensions of the microcrystal, as it has been reported that Bi MR is strongly dependent on size due to mean free path limitation at low temperatures.[39,42] Despite this limitation, microscale bismuth devices still present very high MR values, making them excellent candidates for magnetic field sensing applications.[43]

2.4.2. Anisotropy in Shubnikov-De Haas Oscillations

The most significant indication of anisotropy observed in this study is the variation in the SdH oscillations among the distinct sample types. The frequency f of these oscillations is directly proportional to the area of the cross-section of the Fermi surface S_F with the plane normal to the magnetic field and related to it by Equation (1):

$$S_F = \frac{2\pi e}{\hbar} f \qquad (1)$$

where e is the elementary charge and $\hbar$ Plank's constant divided by 2π. As outlined in the introduction, the Fermi surface of bismuth is highly anisotropic, composed of one hole pocket and three electron pockets.[4,14] Therefore, different periods are expected for the different charge carriers depending on the projection of the Fermi surface on the plane perpendicular to $\vec{B}$. In the case of H samples, $\vec{B}$ is parallel to the trigonal axis and perpendicular to the current direction. Under this configuration, the cross-section of S_F for both hole and electron pockets are similar. Consequently, a single oscillation with a fixed frequency $f \approx f_e \approx f_h$ is expected.

In contrast, for the V samples, the orientation leads to differing cross-sectional areas for each carrier type, resulting in a superposition of oscillations with multiple frequencies.[39]

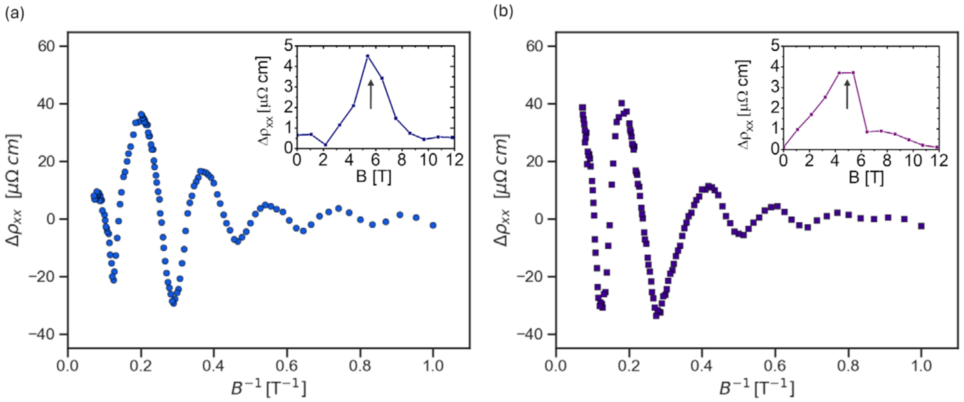

Figure 7. Oscillatory component $\Delta\rho_{xx}$ of the longitudinal resistivity for samples a) H-C and b) H-P, plotted as a function of the inverse of the magnetic field B. Inserts: FFTs of $\Delta\rho_{xx}$ (B), where the main frequency peak has been highlighted with an arrow.

This behavior is reflected in the results presented in this section, which focuses on the H samples. The corresponding results for the V samples are provided in section S5 (Supporting Information). Both H-C and H-P present longitudinal resistivity SdH oscillations from 2 to 15 K for $B > 1$ T. Although none are apparently observed on the $\rho_{xx}(B)$ curve, they are hidden due to the large MR. To extract the oscillatory component $\Delta\rho_{xx}$ the background must be removed. As previously done,[6,7,39] this is achieved by subtracting the longitudinal resistivity curve at 20 K, a temperature at which SdH oscillations are not observed. This method highlights the oscillations which still present a magnetoresistive component due to the differences between the 2 and 20 K resistivity curves. The upper and lower enveloping functions are averaged to remove the remaining MR component to get $\Delta\rho_{xx}$. **Figure** 7 displays the curve $\Delta\rho_{xx}$ (B^{-1}) for H-C (Figure 7a) and H-P (Figure 7b), revealing six full oscillation maxima with decreasing amplitude, which are similar in both samples.

The oscillation frequencies are obtained through fitting the maxima position to a linear function (See figure S6, Supporting Information). The obtained values are 5.6 ± 0.2 T for H-P and 5.8 ± 0.2 T for H-C, values which are in agreement with those obtained by the Fast Fourier Transform (FFT) of $\Delta\rho_{xx}$ (insert in Figure 7a,b), which indicates the presence of only one main oscillation frequency. These frequency values correspond to Fermi surfaces of 5.3 ± 0.2 and 5.5 ± 0.2 10^{12} cm^{-2} for H-P and H-C respectively, values comparable to those previously reported in the literature.[39,42] The $\Delta\rho_{xx}$ (B) curves for V-P and V-C are represented in **Figure** 8a,b, respectively. As expected, a superposition of oscillations of different frequencies is observed, as evidenced by the FFTs displayed in the inserts.

Figures 7 and 8 demonstrate the reproducibility of the method, with samples of the same orientation showing similar behaviors. Additionally, the presence of different oscillation frequencies in V samples is clearly observed, specifically on V-C, where it is visually appreciated.

These results give evidence for the success of the different fabrication methods, showing no relevant differences between C and P methods, in terms of reproducibility and disclosing the anisotropic behavior of magnetotransport properties in Bi. Additionally, the observation of pronounced and reproducible quantum oscillations in Bi crystals indicates a highly pure crystal, proving once again that the damage produced by FIB is not affecting its bulk properties.

The developed methods (P and C) are applicable to other materials with low melting temperatures. Both approaches enable efficient extraction while preserving the crystalline structure and

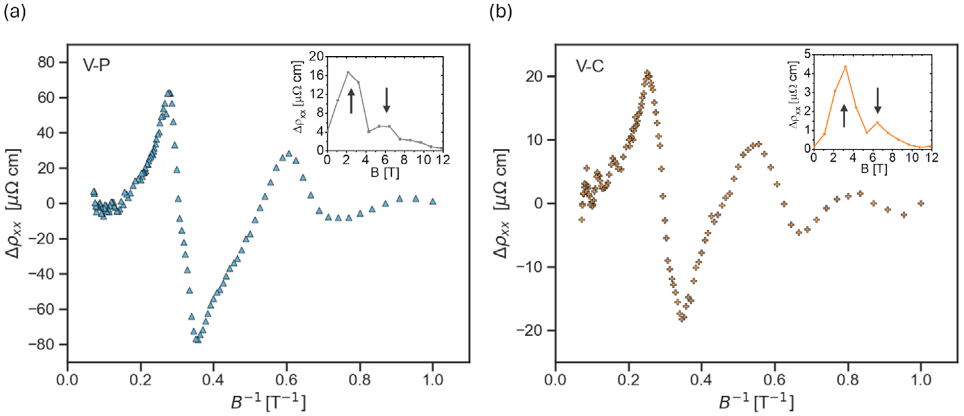

Figure 8. Shubnikov-de Haas oscillations in a) V-P and b) V-C. Inserts represent the FFTs of each curve with the main frequency peaks indicated by arrows.

electronic properties of the material under study. The choice of fabrication method, which does not affect the quality of the results, depends on the required temperature to prevent droplet formation. For materials that require temperatures below –60 °C, the C method is employed. However, if a Peltier stage provides sufficient cooling, as is the case with bismuth, the P method is faster and easier to implement, making it the preferred option. Moreover, this methodology establishes the basis for fabricating hybrid devices that integrate these quantum materials with superconductors, which could facilitate the induction of topological superconductivity.[29]

3. Conclusion

We report anisotropic magnetotransport measurements of four devices fabricated by the extraction of microscale single crystal slabs from a macroscale bismuth single crystal. To study the anisotropy, slabs are extracted in two different orientations relative to the surface of the bulk crystal: horizontal (H) and vertical (V).

The extraction, device fabrication, and electrical contact placement processes are carried out in an equipment combining in situ FIB technologies and SEM, with real-time fabrication control. This approach eliminates the need for chemical resists and removes the necessity of using multiple fabrication techniques.

Due to the visual observation of melting in Bi caused by a local increase in temperature resulting from Ga^+ FIB irradiation, the extraction process is carried out at low temperatures. Two methods have been tested for the process. Method P employs a Peltier plate, lowering the temperature down to –60 °C. Method C employs a nitrogen-based cryo-module which can cool down the samples to reach –150 °C. Based on HRTEM analysis and magnetotransport measurements, no significant differences were observed between samples fabricated using the C and P methods. Therefore, the P method is considered more suitable, as it requires less fabrication time and involves a simpler setup, enabling more efficient sample manipulation.

HRTEM diffraction patterns confirm the crystallographic structure and orientation of our devices, with micrographs showing no relevant damage to the single crystal slabs caused by FIB. H samples present the largest damaged volume, combining amorphized areas and recrystallized areas, which represents less than 10% of the total volume, confirming that our fabrication method is suitable for the research of anisotropic electrical transport properties on bulk single crystals, which are sensitive to local temperature increases due to FIB irradiation.

The studied devices present the expected dependence of longitudinal resistivity with temperature for single-crystal bulk bismuth, exhibiting a metallic behavior. The dependence is linear from 300 to 100 K, changing at low temperatures, where the mean free path of bismuth is of the order of the dimensions of our samples.

The length of the mean free path also affects the $\rho_{xx}(B)$ curves, which change their behavior over 100 K, becoming parabolic. At 300 K, signs of anisotropic electrical transport properties are observed, with H samples exhibiting a broad parabolic $\rho_{xx}(B)$ dependence, whereas V samples show a small inverse peak between –1 T and 1 T.

Lastly, SdH oscillations are observed in both H and V devices, though with different oscillation periods. H samples exhibit a single oscillation frequency, which is consistent with the cross-sectional area of the Fermi surface for their crystallographic orientation. The presence of pronounced SdH oscillations indicates high crystalline quality and purity, further confirming the effectiveness of the fabrication method.

4. Experimental Section

The structure and orientation of the bulk Bi crystal were studied by high-resolution X-ray diffraction in a Bruker D8 Advance diffractometer using parallel-beam optics and monochromatic Cu-Kα_1 radiation (wavelength λ = 1.5406 Å).

Samples were fabricated using a Dual Beam Helios Nanolab 650 System from Thermo Fisher Scientific (Hillsboro, Oregon, USA) belonging to the Laboratory of Advanced Microscopies (LMA) in Zaragoza, Spain. It was equipped with a vertical SEM column that generates electrons by a field emission gun. Tilted at 52° with respect to the electron beam there was a Ga^+ FIB, where ions were generated by a Liquid Metal Ion Source (LIMIS). The beams converge in a sample processing chamber where either the Peltier module or the cryo stage from the cryo module can be installed. The Peltier stage was the Micro Heating and Cooling Stage (MHCS) from Kleindiek Nanotechnik (Reutlingen, Baden–Württemberg, Germany) and the cryo module was the PP3010T Cryo-SEM Preparation System from Quorum (Laughton, East Sussex, UK).

Installed within the sample chamber there was also an Omniprobe nanomanipulator from the brand Oxford Instruments (Abingdon, Oxfordshire, UK), along with several Gas Injection Systems (GIS) for FIBID. Among them, the most relevant to the current work was the Pt precursor GIS ($(CH_3)_3(CpCH_3)$ Pt).

The devices were placed on a silicon chip with a thin thermally grown silicon dioxide layer. Electrical transport measurements were carried out in a Physical Property Measuring System (PPMS) from Quantum Design. It was a commercial equipment belonging to the University of Zaragoza and consists of a cryostat equipped with a superconducting magnet coil capable of reaching fields of 14 T. The system was supplied with He-4 to reach a minimum temperature of 2 K. However, if He-3 insert was used, it can go down to 0.35 K. Samples were introduced inside the cryostat fixed to a specific puck designed for the system. The silicon chips were glued to the puck using a vacuum-resistant glue (G varnish, GE/IMI 7031 Varnish from CMRdirect) and bonded via microscale aluminum wires placed by a micro-bonding equipment.

HRTEM experiments were conducted on a Tecnai F30 (Thermo Fisher Scientific). This equipment had a maximum acceleration voltage of 300 kV and a resolution of 0.19 nm.

Supporting Information

Supporting Information is available from the Wiley Online Library or from the author.

Acknowledgements

The authors are grateful to R. Gracia-Abad, who greatly contributed to the development of the V sample fabrication method. The authors would also like to thank the Laboratory for Advanced Microscopies (LMA) and the Institute of Nanoscience and Materials of Aragón (INMA), from CSIC–Universidad de Zaragoza, for providing access to their instruments and expertise. Additionally, the authors are grateful to the ELECMI network for granting free access through a competitive call to the Helios 650 system through project ELC529-2025. Technical support from the LMA technicians at Universidad de Zaragoza is acknowledged, with special thanks to L. Casado for her assistance with the nanofabrication procedures involving the Dual Beam system. Additionally, the Physical Measurements Service from Servicio General de Apoyo a la Investigación (SAI) at the University of Zaragoza is also acknowledged. Lastly the authors would like to acknowledge the following founding sources: grant PID2020-112914RB-I00 and PID2023-146451OB-I00, funded by MCIN/AEI/10.13039/501100011033 and CSIC through Research Platform PTI-001; the doctoral fellowship for A.S.H. PRE2022-103314, associated with the CSIC project CEX2021-001144-S-20-9, funded by MCIN/AEI/10.13039/501100011033; grant E13_23R, funded by Gobierno de Aragón; and grant CEX2023-001286-S funded by MICIU/AEI/10.13039/501100011033.

Conflict of Interest

The authors declare no conflict of interest.

Data Availability Statement

The data that support the findings of this study are available from the corresponding author upon reasonable request.

Keywords

bismuth, cryogenic milling, focused ion beam, magnetotransport, microcrystal, Shubnikov-de Haas

Received: July 8, 2025
Revised: July 31, 2025

[1] Y. Tokura, M. Kawasaki, N. Nagaosa, *Nature Phys* **2017**, *13*, 1056.
[2] A. Acín, I. Bloch, H. Buhrman, T. Calarco, C. Eichler, J. Eisert, D. Esteve, N. Gisin, S. J. Glaser, F. Jelezko, S. Kuhr, M. Lewenstein, M. F. Riedel, P. O. Schmidt, R. Thew, A. Wallraff, I. Walmsley, F. K. Wilhelm, *New J. Phys.* **2018**, *20*, 080201.
[3] M. Ziese, H. J. Blythe, *J. Phys.: Condens. Matter* **2000**, *12*, 13.
[4] Z. Zhu, B. Fauqué, K. Behnia, Y. Fuseya, *J Phys Condens Matter* **2018**, *30*, 313001.
[5] N. K. Karn, Y. Kumar, G. Awana, V. P. S. Awana, *physica status solidi* **2025**, *262*, 2400077
[6] F. Y. Yang, K. Liu, K. Hong, D. H. Reich, P. C. Searson, C. L. Chien, Y. Leprince-Wang, K. Yu-Zhang, K. Han, *Phys. Rev. B* **2000**, *61*, 6631.
[7] C. L. Chien, F. Y. Yang, K. Liu, D. H. Reich, P. C. Searson, *J. Appl. Phys.* **2000**, *87*, 4659.
[8] Y. Fuseya, M. Ogata, H. Fukuyama, *J. Phys. Soc. Jpn.* **2015**, *84*, 012001.
[9] H.-H. Sun, M.-X. Wang, F. Zhu, G.-Y. Wang, H.-Y. Ma, Z.-A. Xu, Q. Liao, Y. Lu, C.-L. Gao, Y.-Y. Li, C. Liu, D. Qian, D. Guan, J.-F. Jia, *Nano Lett.* **2017**, *17*, 3035.
[10] S. Murakami, *Phys. Rev. Lett.* **2006**, *97*, 236805.
[11] F. Schindler, Z. Wang, M. G. Vergniory, A. M. Cook, A. Murani, S. Sengupta, A. Y. Kasumov, R. Deblock, S. Jeon, I. Drozdov, H. Bouchiat, S. Guéron, A. Yazdani, B. A. Bernevig, T. Neupert, *Nature Phys* **2018**, *14*, 918.
[12] L. V. Shubnikow, W. J. de Haas, *Leiden Commun.* **1930**, *207*, 35.
[13] W. J. De Haas, P. M. Van Alphen, *Proc. Netherlands Roy. Acad. Sci.* **1930**, *33*, 170.
[14] R. Akiyama, K. Sumida, S. Ichinokura, R. Nakanishi, A. Kimura, K. A. Kokh, O. E. Tereshchenko, S. Hasegawa, *J. Phys.: Condens. Matter* **2018**, *30*, 265001.
[15] P. Hofmann, *Prog. Surf. Sci.* **2006**, *81*, 191.
[16] P. J. W. Moll, *Annu. Rev. Condens. Matter Phys.* **2018**, *9*, 147.
[17] K. Höflich, G. Hobler, F. I. Allen, T. Wirtz, G. Rius, L. McElwee-White, A. V. Krasheninnikov, M. Schmidt, I. Utke, N. Klingner, M. Osenberg, R. Córdoba, F. Djurabekova, I. Manke, P. Moll, M. Manoccio, J. M. De Teresa, L. Bischoff, J. Michler, O. De Castro, A. Delobbe, P. Dunne, O. V. Dobrovolskiy, N. Frese, A. Gölzhäuser, P. Mazarov, D. Koelle, W. Möller, F. Pérez-Murano, P. Philipp, et al., *Appl. Phys. Rev.* **2023**, *10*, 041311.
[18] J. M. De Teresa, P. Orús, R. Córdoba, P. Philipp, *Micromachines 2019* **2019**, *10*, 799.
[19] H. Yang, M. Schmidt, V. Süss, M. Chan, F. F. Balakirev, R. D. McDonald, S. S. P. Parkin, C. Felser, B. Yan, P. J. W. Moll, *New J. Phys.* **2018**, *20*, 043008.
[20] J. Jaroszynski, F. Hunte, L. Balicas, Y. Jo, I. Raičević, A. Gurevich, D. C. Larbalestier, F. F. Balakirev, L. Fang, P. Cheng, Y. Jia, H. H. Wen, *Phys. Rev. B* **2008**, *78*, 174523.
[21] M. D. Bachmann, A. L. Sharpe, G. Baker, A. W. Barnard, C. Putzke, T. Scaffidi, N. Nandi, P. H. McGuinness, E. Zhakina, M. Moravec, S. Khim, M. König, D. Goldhaber-Gordon, D. A. Bonn, A. P. Mackenzie, P. J. W. Moll, *Nat. Phys.* **2022**, *18*, 819.
[22] N. Mathur, F. S. Yasin, M. J. Stolt, T. Nagai, K. Kimoto, H. Du, M. Tian, Y. Tokura, X. Yu, S. Jin, *Adv. Funct. Mater.* **2021**, *31*, 2008521.
[23] S. Mishra, Y. Liu, E. D. Bauer, F. Ronning, S. M. Thomas, *Phys. Rev. B* **2022**, *106*, L140502.
[24] P. J. W. Moll, R. Puzniak, F. Balakirev, K. Rogacki, J. Karpinski, N. D. Zhigadlo, B. Batlogg, *Nature Mater* **2010**, *9*, 628.
[25] P. J. W. Moll, B. Zeng, L. Balicas, S. Galeski, F. F. Balakirev, E. D. Bauer, F. Ronning, *Nat. Commun.* **2015**, *6*, 6663.
[26] E. Mikheev, T. Zimmerling, A. Estry, P. J. W. Moll, D. Goldhaber-Gordon, *Nano Lett.* **2022**, *22*, 3872.
[27] J. Diaz, K. Wang, J. Straquadine, C. Putzke, Q. Yang, B. Yan, S. L. Bud'ko, P. C. Canfield, P. J. W. Moll, *Nat. Commun.* **2024**, *15*, 4585.
[28] Y. Guan, F. Komori, M. Horio, A. Fukuda, Y. Tsujikawa, K. Ozawa, M. Kamiko, D. Nishio-Hamane, T. Kawauchi, K. Fukutani, Y. Tokumoto, K. Edagawa, R. Tamura, I. Matsuda, *Jpn. J. Appl. Phys.* **2024**, *63*, 030906.
[29] R. Gracia-Abad, S. Sangiao, G. Balakrishnan, J. M. De Teresa, *Sci. Rep.* **2024**, *14*, 24294.
[30] A. Sáenz-Hernández, S. Sangiao, G. Balakrishnan, J. M. De Teresa, *MRS Commun.* **2025**, *15*, 414.
[31] N. Marcano, S. Sangiao, J. M. De Teresa, L. Morellón, M. R. Ibarra, M. Plaza, L. Pérez, *J. Magn. Magn. Mater.* **2010**, *322*, 1460.
[32] K. A. Grossklaus, J. M. Millunchick, *J. Appl. Phys.* **2011**, *109*, 014319.
[33] Q. Wei, J. Lian, W. Lu, L. Wang, *Phys. Rev. Lett.* **2008**, *100*, 076103.
[34] M. C. Dolph, C. Santeufemio, *Nucl. Instrum. Methods Phys. Res., B* **2014**, *328*, 33.
[35] M. Otsuka, H. Morita, T. Arisaka, Y. Hasegawa, *J. Appl. Phys.* **2022**, *131*, 214302.
[36] Y. Hasegawa, D. Yamashita, *Jpn. J. Appl. Phys.* **2022**, *61*, 065005.
[37] Z. Zhang, X. Sun, M. S. Dresselhaus, J. Y. Ying, J. Heremans, *Phys. Rev. B* **2000**, *61*, 4850.
[38] Y. Hasegawa, D. Yamashita, *Jpn. J. Appl. Phys.* **2022**, *61*, 065005.
[39] F. Y. Yang, K. Liu, K. Hong, D. H. Reich, P. C. Searson, C. L. Chien, *Science* **1999**, *284*, 1335.
[40] P. Ritzinger, K. Výborný, *R. Soc. Open Sci.* **2023**, *10*, 230564.
[41] R. Niu, W. K. Zhu, *J. Phys.: Condens. Matter* **2022**, *34*, 113001.
[42] L. Chen, A. X. Wu, N. Tulu, J. Wang, A. Juanson, K. Watanabe, T. Taniguchi, M. T. Pettes, M. A. Campbell, M. Xu, C. A. Gadre, Y. Zhou, H. Chen, P. Cao, L. A. Jauregui, R. Wu, X. Pan, J. D. Sanchez-Yamagishi, *Nat. Mater.* **2024**, *23*, 741.
[43] E. S. Oliveros-Mata, C. Voigt, G. S. Cañón Bermúdez, Y. Zabila, N. M. Valdez-Garduño, M. Fritsch, S. Mosch, M. Kusnezoff, J. Fassbender, M. Vinnichenko, D. Makarov, *Adv. Mater. Technol.* **2022**, *7*, 2200227.